

Micro- to nano-scale areal heterogeneity in pore structure and mineral compositions of a sub-decimeter-sized Eagle Ford Shale

Qiming Wang^a, Qinhong Hu^{a, *}, Chen Zhao^a, Xiaoguang Yang^{a,b}, Tao Zhang^a, Jan Ilavsky^c, Ivan Kuzmenko^c, Binyu Ma^d, and Yukio Tachi^e

^a Department of Earth and Environmental Sciences, the University of Texas at Arlington, TX 76019, USA

^b School of Energy Resources, China University of Geoscience (Beijing), Beijing, 100083, China

^c X-ray Science Division, Advanced Photon Source, Argonne National Laboratory, Lemont, IL 60439

^d Shandong Provincial Key Laboratory of Deep Oil and Gas, China University of Petroleum (East China), Qingdao 266580, China

^e Department of Geological Disposal Research, Japan Atomic Energy Agency, Ibaraki-ken, 319-1194, Japan.

Prepared for:

Journal of Geophysical Research - Solid Earth

April 17, 2022

* Corresponding author: maxhu@uta.edu

Key Words: Eagle Ford Shale, X-ray scattering, pore structure, -XRF, heterogeneity

Key Points (140 character limit including spaces):

- An areal heterogeneity was studied by multiple approaches on two sub-decimeter-sized samples of fine-grained Eagle Ford Shale.
- Pore structure of nm- m-scaled pore sizes mapped by SANS are coupled with petrography, porosimetry, mineralogy, and organic geochemistry.
- Areal heterogeneity of porosity distribution and sedimentary features is derived at our sampling and analytical scales.

Abstract (250 word limit)

To improve the understanding of spatial heterogeneity in fine-grained shale, methods of microscale X-ray fluorescence (-XRF) mapping, (ultra-) small-angle x-ray scattering [(U)SAXS] and wide-angle X-ray scattering were used to determine elemental and pore structure variations in sizes up to ~10 cm on two samples prepared at circular (8 cm×8 cm×0.8 mm in width×length×thickness) and rectangular (5 cm×8 cm×0.8 mm) orientations from a piece of Eagle Ford Shale outcrop in South Texas. Thin section petrography and field emission-scanning electron microscopy, X-ray diffraction (XRD), total organic carbon,

and pyrolysis were also utilized to investigate the potential spatial heterogeneity of pore types, mineral and organic matter compositions for both samples. Overall, the siliceous-carbonate mineral contents in these carbonate-rich Eagle Ford Shale vary between laminations at mm scales. For the circular sample, porosity and surface area variations range from 0.82 to 3.04% and 1.51 to 14.1 m²/g, respectively. For the rectangular sample, values for porosity and surface area vary from 0.93 to 2.50% and 3.95 to 10.8 m²/g. By analyzing six selected sub-samples on each of two samples with X-ray scattering and XRD techniques, nm-sized pores are mainly interparticle ones in the higher calcite regions, where the porosity is also relatively lower, while the lower calcite regions consist of both interparticle and intraparticle pore types with higher porosity. Finally, the μ -XRF and (U)SAXS are combined to generate porosity distribution maps to provide more insights about its heterogeneity related to the laminations and fractures at our observational scales.

Plain Language Summary

Geological samples have a wide range of heterogeneity at different sampling and analytical scales. Cores are usually analyzed after plugging, cutting, and/or crushing which will lead to the issues of inability of studying, and altering, the heterogeneity at the decimeter-scale. This study investigates the areal heterogeneity of mineral compositions, pore structure, and organic matter composition on two sub-dm-sized samples from an outcrop of Eagle Ford Shale. Complementary and integrated approaches of X-ray fluorescence for microscale mapping, (ultra-) small-angle x-ray scattering for pore structure characterization of pore diameters at 1-1000 nm, and wide-angle X-ray scattering for mineral types, in addition to thin section petrography, field emission-scanning electron microscopy, X-ray diffraction, total organic carbon analyses, and pyrolysis, were utilized to investigate the spatial heterogeneity of pore types, mineral and organic matter compositions to derive the correlation of porosity distribution and sedimentary features. This work illustrates the capabilities of relatively quick and non-destructive sampling of dm-scaled sizes and analytical scales of m-cm for areal heterogeneity studies of natural rocks in various geophysical applications.

1. Introduction

Successful and economical recovery of gas and oil from shale has become one of the hottest geological topics in recent years. Compared to conventional sandstone reservoirs, shale is well known for its complex pore systems and high heterogeneity from nanometer to basin scales (Peng et al., 2017; Borrok et al., 2019; Ma et al., Mighani., 2019; Zhang et al., 2019; Huang et al., 2020). Complementary with wireline log and seismic data, core analyses are a direct measurement of rock properties. However, they are limited by their resolution and sample holding capacity of various measurement approaches and associated instrumentation. Cores are usually analyzed after plugging, cutting, and/or

crushing which will lead to the issues of inability of studying, and altering, the heterogeneity at the dm-scale. With the improvement in instrumentation, a variety of non-destructive techniques is available to assess the pore structure and geochemical properties of core-sized (commonly 2.5 cm in diameter) samples. Microscale X-ray fluorescence (-XRF) mapping has been applied in core-sized samples to visualize the elemental and laminar distribution (Reed et al., 2019; Birdwell et al., 2019; Barker et al., 2020a; 2020b). Wang et al. (2021b) recently applied a rapid and high-precision (ultra) small-angle X-ray scattering [(U)SAXS] technique to characterize the porosity, pore size distribution, surface area and their distribution in a Barnett Shale sample across an area of several tens of cm².

The Cretaceous Engle Ford Shale is a prolific petroleum reservoir in the central to southwest Texas region (U.S. Energy Information Administration, 2022). The organic matter-rich beds of the Eagle Ford Formation have been extensively studied with regard to depositional environment, diagenesis, mineral composition, organic matter type, pore types and pore-size distribution, and water-rock interaction (e.g., Pommer and Milliken, 2015; Frebourg et al., 2016; Alnahwi and Loucks., 2018; Wang et al., 2021a). These studies indicate a high degree of heterogeneity across multiple observational scales. At the field scale across several counties, the organic matter (OM)-rich beds are interbedded with OM-poor limestones, and the proportion of OM-rich shale vs. limestone negatively influences the formation fracability and positively the petroleum production (Breyer et al., 2015). On the core scale of centimeters, the Eagle Ford Shale shows a lithologic variation from coccolith-rich pellets to siliceous-argillaceous seams, and foraminifera (Reed et al., 2019), and there are still many remaining needs for further investigation into larger-sized samples for the decimeter-scale variability in properties such as pore structure, mineral and OM composition.

This work has employed -XRF mapping, (U)SAXS, and wide-angle X-ray scattering (WAXS) to investigate the spatial heterogeneity of the elemental & mineralogical composition and pore structure on two Eagle Ford Shale wafers taken perpendicular to each other. Then, six locations on each sample (1 cm×1 cm×0.8 mm) showing large variations in pore structure and elemental composition were selected and cut into chips. These sub-samples were processed at different sizes for analyses by petrographic microscopy, field emission-scanning electron microscopy (FE-SEM), X-ray diffraction (XRD), total organic carbon content (TOC), and pyrolysis to investigate the spatial heterogeneity of sedimentary structure, mineral composition, pore types, organic richness, and thermal maturity.

2. Methods

2.1 Sample collection and preparation

A Cretaceous-aged Eagle Ford Shale sample was collected from an outcrop outside of Del Rio city, TX. First the outcrop was cored as a cylinder at 10.2 cm in diameter and 10 cm in height, and then two samples perpendicular to each other

were cut at a thickness of 0.8 mm (Fig 1A); both samples are perpendicular to the bedding plane of the original outcrop. The circular sample (C sample in later texts) shown in Fig. 1B has a diameter of 10.2 cm, and the rectangular sample (R sample) shown in Fig. 1C has a dimension of 10.2 cm×6.1 cm. Samples were placed in an oven at 60 C° for 2 days to remove the moisture in the connected pore space before analyses. Both μ -XRF mapping and X-ray scattering were first carried out on these C and R whole samples, and then selected locations were cut into 1cm×1cm×0.08 mm sub-samples (orange squares in Fig. 1B-C) for X-ray diffraction (XRD) analyses and scanning electron microscopy (SEM) imaging, and crushed to powder for the analyses of total organic carbon (TOC) and pyrolysis. The rock chips shown in blue rectangular (Fig. 1B-C) were prepared to make four thin sections for petrography. The rest of rock samples in orange squares and blue rectangles were ball-milled as powders for bulk XRD analyses.

2.2 X-ray scattering

Both ultra-small angle X-ray scattering (USAXS) and small-angle X-ray scattering (SAXS) were conducted on the C and R samples to investigate the areal heterogeneity of porosity, pore size distribution, and surface area distribution over a pore-diameter scale of 1-1000 nm, and wide-angle X-ray scattering (WAXS) was used to determine the mineral types. USAXS/SAXS/WAXS analyses were conducted at 9-ID beamline of Advanced Photo Source (APS) at Argonne National Laboratory. The detailed beamline parameters, fundamental principles, analyses procedure, and data processing follow the work of Ilavsky and Jemian (2009), Ilavsky et al. (2018), and Wang et al. (2021b). For the C sample, a total of 37 positions were scanned (Fig. 1B), with each position scanned at 3-4 beam spots (labeled as A to C-D) following the sequence in Wang et al. (2021b) for a total of 132 beam spots being scanned. For the R sample, there was 30 positions (Fig. 1C), and each position was scanned at 2-3 beam spots for a total of 72 beam spots. Each beam spot only took 90, 10, and 10 seconds to complete the sequential runs of USAXS and SAXS (for pore structure) & WAXS (for mineral composition). Hereafter individual beam spots are described as, for example, Position 1A or Position 2B, where the former refers to Position 1 & beam spot A, and the latter to Position 2 & beam spot B. In brief summary, the USAXS and SAXS are combined to be (U)SAXS to determine the porosity, pore diameter distribution, and surface area, at beam spots of 0.8 mm×0.8 mm, and the WAXS is used to determine the type of minerals, at the same beam spots but a smaller area of 0.8 mm×0.2 mm.

2.3 Micro-X-ray Fluorescence Mapping

μ -XRF mapping is a fast and non-destructive method that can quantitatively measure the spatial elemental distribution on the surface of mm to cm-sized samples (Nikonow and Rammelmair, 2016; Birdwell, et al., 2018). Our data were obtained from a μ -EDXRF spectrometer M4 Tornado manufactured by Bruker, and the chemical elements Al, Ca, Fe, K, Mg, Mn, Na, and Si were selected to be monitored at 50 kV. The maximum resolution of μ -XRF scanning

is 14 μm , and the scanning time depends on the sample size and resolution. For the sub-dm-sized samples used here with the best resolution, the scanning time is around 20 hours.

2.4 Petrographic microscopy

To investigate the changes in sedimentary textures for C and R samples, a rectangular area of $\sim 2\text{ cm} \times 10\text{ cm}$ on both samples was cut out for petrographic microscopy (Fig. 1B-C), and the photos of prepared thin sections were taken under the Leica DM 750P polarizing microscope.

2.5 X-ray diffraction

After X-ray scattering and $\mu\text{-XRF}$ mapping for pore structure and elemental composition of the large-sized C and R samples, six sub-samples as rock chips ($1\text{ cm} \times 1\text{ cm} \times 0.8\text{ mm}$) from areas showing large variations were selected and cut out from each sample, in order to determine the mineral compositions by XRD on the intact sample. In addition, a ball-milled powder sample from the rest of rock chips after cutting of twelve sub-samples was prepared to investigate the average mineral composition of the sample. The XRD analyses were conducted on a Shimadzu MaximaX XRD-7000, and the 2θ was set to be 20 to 70 degrees. The Jade 9 analysis program was used to determine the mineral compositions from the raw spectral data.

2.6 Field emission-scanning electron microscopy

Six selected sub-samples on each of C and R samples were gradually polished with sandpapers ranging from 200, 400, 800, 1200, 2000, and 3000 grits. After polishing, samples were coated with Au/Pt in CrC-100 Sputtering system and then directly examined by Hitachi 4800 SEM to investigate the pore types. In this study, images were collected with the secondary electrons (SE) mode under 15 kV for minerals and their related pores and 1.5 kV for organic matters-hosted pores.

2.7 TOC and pyrolysis

When the previous analyses were finished, these 12 selected sub-samples from C and R samples were crushed to be powders ($< 75\ \mu\text{m}$) to examine the organic matter content (TOC) by LECO C230 Carbon Analyzer, as well as quality and thermal maturity through HAWK pyrolysis manufactured by Wildcat Technologies.

3. Results

3.1 Areal heterogeneity of sub-decimeter-sized samples

3.1.1 Elemental distribution

The results of powder-sized samples show the average mineral compositions of the whole sample (Table 1). These results indicate that the samples used in this study are carbonate-rich with small amounts of quartz and a very small amount of pyrite & clay minerals. Therefore, in the following $\mu\text{-XRF}$ mapping

test, only the elemental composition data related to the detected main minerals are presented, with tight elements selected.

In XRF images (Figs. 2-3), the higher the concentration is, the brighter the color is. Based on the mineral compositions provided by XRD results for the powder sample, Ca being detected by the -XRF is present only in calcite (CaCO_3), Fe is in pyrite (FeS_2), Si is from siliceous minerals such as quartz (SiO_2) and clay minerals, and Al, Na & K are present in clay minerals. Since the clay minerals only account for a very small amount of the total minerals (Table 1), the Si signal will be mostly due to quartz, so the detection of Al, Na, and K is used to characterize the clay minerals distribution. Both Mg and Mn are used to reflect the potential presence of ankerite [$\text{Ca}(\text{Fe}, \text{Mg}, \text{Mn})(\text{CO}_3)_2$] or dolomite [$\text{CaMg}(\text{CO}_3)_2$]. For both C and R samples (Figs. 2-3), strong laminations are seen for high concentrations of Ca, Si, and Fe, slight laminations are observed for Al and K, and no laminations are present for Mg, Mn, and Na. To quantify the distribution of three most abundant elements (Ca, Si, and Fe), the intensities of scanned areas are normalized to the highest intensity observed for each element (Fig. 4). In Fig. 4A, the normalized Ca distribution map of the C sample shows that Ca is rich in all scanned areas with multiple laminations across the sample. The difference in the relative intensity (RI) between higher Ca areas (yellow color, ~80% RI) and lower Ca (green color, ~60%) area is relatively small. The area with higher Ca concentrations is in the upper two-thirds of the sample, whereas the lower Ca concentrations occur in the bottom portion of one-third (Fig. 4A). The normalized Si distribution map (Fig. 4B) shows that areas with higher Si concentration are located at the sample bottom, and lower Si concentrations occur in the middle and upper regions of the sample. The normalized distribution map for Fe (Fig. 4C) shows very high intensity (~80-100% RI) at the sample bottom, but only a low intensity (~0-20% RI) for the rest of the sample.

For the normalized distribution maps of the R sample (Fig. 4D-F), the areas with higher Ca concentrations (~60-100% RI) appear in the middle of sample, while the areas with lower Ca concentrations (~0-20% RI) are located on the left and right sides (Fig. 4D). The higher concentration areas of Si (~80-100% RI) and Fe (~60%-100% RI) occur on the right-hand side (Fig. 4E-F). A comparison of these three normalized maps shows that the area with high RI for Ca also has low concentrations of Si and Fe; similarly, the area with low Ca concentration has high Si and Fe concentrations.

Once the Ca, Si, and Fe data are normalized, the sedimentary features, such as laminations and fractures, can be identified and marked on Figs. 4G and H for the C and R samples, respectively. In Fig. 4G, several fractures cut through the laminations in the C sample and offset the laminations on the right side by 3-5 m. In the R sample (Fig. 4H), fractures cut through the laminations and lead to an offset of laminations.

3.1.2 Sedimentary textures

Thin section petrography was carried out to determine the textural and mineral compositional changes across two C and R samples. Four positions with different Si/Ca ratios (following the normalized map in Fig. 4) on each sample were selected for petrographic microscopy (Fig. 5). Thin sections of the small rectangular areas marked as A-H in Fig. 5 are shown in Fig. 6A-H. Under a plane-polarized light, these sub-samples show as either yellow (calcite) and brown-black color (quartz, clay, pyrite, and organic matter). Unlike other fossil-rich Eagle Ford Shale samples being collected from both wells and outcrop (Pommer and Milliken, 2015; Lehrmann et al., 2019; Reed et al., 2019; Wang et al., 2021a), fossils are only occasionally found in this sample. In the high Ca regions (A and E), the yellow color is dominant, whereas in the high Si regions (D and H), the proportion of brown-black color increases dramatically. In other thin section views cutting across Ca-Si mixed laminations (B, C, F, and G), the ratios of yellow/brown-black are intermediate. Based on the thin section petrographic observations, the samples do not show a lithological change at sub-cm scales, though there is a variation in compositions, evidenced from different ratios of yellow/black-brown colors.

3.1.3 Pore structure

The pore structure of the C and R samples was investigated with (U)SAXS techniques. The porosity distribution and surface area for each sample are presented in Fig. 7. Overall, the porosity of the C sample ranges from 0.82 to 3.04%, with an average of $1.72 \pm 0.36\%$ (N=132). The high porosity region is mainly located at the bottom region. The porosity of the R sample ranges from 0.93 to 2.50% and has an average of $1.61 \pm 0.35\%$ (N=72). The high porosity region occurs at the right and bottom regions. The surface area distribution of these two samples is spatially mapped out as well from (U)SAXS data. The surface area of the C sample is 1.51-14.1 m^2/g with an average of $6.52 \pm 1.74 \text{ m}^2/\text{g}$ (N=132), similar to the R sample of $6.89 \pm 1.52 \text{ m}^2/\text{g}$ (N=72). While the distributions of porosity and surface area are similar, there are still some differences. For example, Positions 11 (coordinates: x=6 and y=6) and 20 (coordinates: x=4 and y=6) have the lowest porosities on the C sample, but their surface areas are not the lowest (Fig. 7 A and C). For the R sample, Positions 27 (coordinates: x=2 and y=0) and 30 (coordinates: x=8 and y=0) do not show the highest porosity, but they have the highest surface area (Fig. 7B and D)

3.2 Areal heterogeneity of selected sub-samples of large C and R samples

This section looks at the differences in mineral compositions, pore types, organic matter quantity (TOC) and quality (pyrolysis), as well as their influences on the pore size and surface area distributions. Six sub-samples (1 cm \times 1 cm \times 0.8 mm) on both C and R samples with high differences in Ca/Si intensity, porosity, and surface area were selected and cut out for XRD and SEM analyses and then crushed to powder for TOC and pyrolysis analyses. WAXS was conducted for the large-sized samples before the rock chips were cut out to validate the XRD results at different sampling scales (XRD: 1 cm \times 1 cm; WAXS: 0.8 mm \times 0.2

mm). For the C sample, a total of six sub-samples were selected from Positions 3 (named C3), 10, 16, 22, 34, and 37. Similarly, six sub-samples from the R sample were chosen from Positions 15, 22, 24, 26, 28, and 30 (Fig. 5; Table 2).

3.2.1 Mineral compositions and organic matters

The results of mineral compositions, TOC, and pyrolysis of these 12 sub-samples are shown in Table 1. Due to their low abundance (0.7% from powder sample), the clay minerals are neglected during the XRD mineral composition calculation, as the calculated values for a very small amount may have a large uncertainty. C3, C10, C16, and C21 have relatively higher calcite (91.7 to 94.8 wt.%) and lower quartz (5.2 to 6.9 wt.%), whereas the C34 and C37 positions have relatively lower calcite (85.6 and 87.0 wt.%) and higher quartz (10.8 and 11.7 wt.%). Pyrite only appears in sub-samples of C16, C21, and C37, with contents ranging from 1.3 to 3.7 wt.%. R22 and R26 show a detection of relatively low quartz (6.3 and 7.6 wt.%), high calcite (93.7 and 92.4 wt.%), and no pyrite. In contrast, R15, R24, R28, and R30 sub-samples show higher quartz (11.1-15.5 wt.%) and lower calcite (82.7-88.9 wt.%). The higher quartz rock-chips are commonly found in sub-samples with more abundant pyrite (ranging from 1.1 to 2.3 wt.%), with an exception of R28. Even though the quantification function for mineral composition from WAXS data has not been developed, its function can help to determine what types of minerals appearing in the sampling location of 0.8 mm \times 0.2 mm. Results show that the higher calcite samples barely contain pyrite along with a low intensity of kaolinite and quartz (Fig. 8A and C), whereas the lower calcite samples have higher intensities of pyrite, kaolinite, and quartz (Fig. 8B and D). In addition, Table 1 shows that TOC values are higher in sub-samples with lower calcite for both R and C samples. The pyrolysis results show that all of 12 sub-samples have low values of S1 (free hydrocarbons) and S3 (CO₂ yield during pyrolysis from kerogen). Low S1 values may be due to the fact that this being an outcrop sample, and free hydrocarbons have evaporated off or been weathered away. The S2 values (mass of hydrocarbons per gram of rock generated during pyrolysis) increase with an increasing TOC content and, therefore, the hydrogen index (HI) ranges from 538 to 769. The T_{max} values (434-435 °C) from the pyrolysis are very similar as would be expected, indicating that this Eagle Ford Shale from outcrop is likely in the very early oil generation stage (Yang and Horsfield, 2020).

3.2.2 Pore types

Fig. 9 presents the SEM images of six sub-samples taken from the C sample (shown in Fig. 5). In the higher calcite sub-samples (C3, C10, C16, and C21; Table 1), the pores are mostly interparticle between calcite and quartz (Fig. 9A, B, and D). In some parts of the solid rock matrix, there is a limited abundance of pores (Fig. 9C). In the sub-samples with lower calcite contents (C34 and C37), the pores are primarily interparticle and intraparticle in types. The interparticle pores appear between calcite, quartz, pyrite, and clay minerals, whereas the intraparticle pores are present inside pyrite framboids and clay aggregates (Fig. 9E-F and H-I). Due to its low maturity, the organic matter does not contain

any pores (Fig. 9G). Similarly, Fig. 10 shows the SEM images of six sub-samples from the R sample. The higher calcite sub-samples (R22 and R26) contain dominantly interparticle pores, and only a few pores appear in the solid matrix (Fig. 10B and D). In the lower calcite sub-samples (R15, R24, R28, and R30), pores are mainly observed between mineral crystals (Fig. 10A and G); in addition, pyrite framboids and clay aggregates can provide pore spaces (Fig. 10E, H, and I). The quartz in the SEM images is mainly secondary (formed as cement during diagenesis) with a good crystal form, indicating that it was probably from dissolved silica and precipitated as quartz cement (Fig. 9B and D; Fig 10E).

3.2.3 Pore structure

Fig. 11 shows the relationship of pore diameter with either incremental porosity or surface area of six beam spots of highest porosity in each subsample for C and R samples, whereas Table 2 gives the total porosity and surface area as well as their distributions. Pores in the C sample are dominated by diameters in the 100-1000 nm range. The higher calcite locations (C3A, C10B, C16A, and C21B; all >91%) show two major peaks in the 200-400 nm and 500-1000 nm ranges, whereas the lower calcite locations (C34A and H37A; <87%) exhibit two major peaks at 100-200 nm and 400-1000 nm. Unlike other locations, the C37A shows two peaks in the 400-1000 nm range. The surface area of all sampling locations mostly falls in the 1-10 nm range, with two main peaks located at 1-4 nm and 5-7 nm. The higher calcite beam spots (C3A, C10B, C16A, and C21B) show similar peaks in intensity and pore diameter range; on the contrary, the lower calcite C34A spot has no peaks between 5-7 nm, and rather a high peak at 10-12 nm. Furthermore, for the R sample, both higher calcite spots (R22A and R26A; >92%) and lower calcite spots (R15A, R24C, R28A, and R30A; <89%) have peaks at similar pore diameters, but they have different intensities and widths. Moreover, the incremental surface areas of six locations have similar peaks but different intensity as well (Fig. 11).

4 Discussion

In this study, the results of -XRF patterns show that the Ca abundance is inversely correlated with Si, Fe, Al, and K (Figs. 2-3) at sub-dm scales. The (U)SAXS results illustrate that the porosity and surface area vary across the whole sample area (Fig. 7). Shales are fine-grained rocks being deposited and accumulated under low-energy aqueous environments, and the depositional process of laminations is a function of the *in situ* water energy and sediment supply (O'Brien 1996; Frébourg et al., 2016; Yawar and Schieber, 2017). In a similar deposition environment, the only difference between adjacent laminations is the type of sediment supply. Fig. 12 shows cross-plots of calcite from XRD vs. porosity [from (U)SAXS], surface area [from (U)SAXS], TOC (from LECO), and S2 (from pyrolysis) of 12 selected sub-samples from the C and R samples. It shows a negative relationship between calcite and porosity (correlation coefficient $R^2=0.7852$; $N=12$), surface area ($R^2=0.4748$), TOC ($R^2=0.7358$), and S2 ($R^2=0.8641$). This negative relationship between calcite and porosity indi-

cates that calcite contents are inversely related to pore space. In addition to pores being observed between the mineral crystals, Louck et al. (2012) reported that pores are also presented in pyrite framboids and clay aggregates. From the XRD results and SEM images in this study, the pyrite and clay minerals are only present in the lower calcite regions. Within the pyrite framboids and clay aggregates, those intraparticle pores provide extra pore spaces and surface area in these lower calcite locations, which lead to higher porosity and surface area compared with higher-calcite spots. Reed et al. (2009) and Frebourg et al. (2016) also pointed out that the recrystallization of calcite will eliminate its original texture and the calcite overgrowth will fill the pore networks, and therefore, porosity will decrease in the higher calcite content regions. In our thin sections photos (Fig. 6 A, C, and H), the calcitic-fossils were dissolved and reprecipitated to be with crystalline calcite and only a couple of molded fossils are visible. Therefore, in the higher calcite spots, the porosity will be expected to be lower than that in the lower calcite spots.

Many other studies also reported that the organic matter can provide a certain amount of porosity to organic matter-rich shale as a result of petroleum generation (Curtis et al., 2012; Ko et al., 2016; İnan et al., 2018; Wang et al., 2020; Bai et al., 2021). However, in this Eagle Ford Shale sample, pyrolysis results indicate that organic matter is at best in the early oil window, and SEM observations show that no pores show up within the organic matter particles. Therefore, the contribution of organic matter-hosted pores to porosity and pore surface area is negligible in this sample. Overall, for this carbonate-rich Eagle Ford Shale, the increase in siliceous minerals and pyrite will lead to high porosity and surface area. Several studies have reported that high porosity is not necessarily related to high silica content (Yang et al., 2016; Wu et al., 2019; Shu et al., 2021), but might be related to clay mineral contents (Ross and Bustin, 2008; Chen et al., 2016). Calcite also shows a weak negative relationship to the surface area, but the R^2 is only 0.4748. It's been recognized that clay minerals have a much higher surface area than calcite and quartz (Clouter et al., 2001; Michot and Villieras, 2006; Montes-Hernandez et al., 2008; Kuila and Prasad, 2013). However, our Eagle Ford Shale sample has a very limited amount of clays (less than 1%) from the XRD analyses. In addition, TOC and S2 show a good negative relationship ($R^2= 0.7358$ and 0.8641) with calcite. Many previous studies suggested that Fe can stimulate organic matter productivity (Tribovillard et al., 2015; Frebourg et al., 2016; Zhang et al., 2017). As with the clay minerals, however, the composition of pyrite cannot be accurately calculated due to its low abundance in this sample.

Since the cross-plot of calcite and porosity shows a good correlation ($R^2=0.7852$), the Ca signals on the XRF maps can be directly correlated to the porosity. Based on the normalized Ca intensity data, the porosity of each lamination can be calculated and shown in Fig. 4G and H. Therefore, the sedimentary textures map (Fig. 4G and H) can be filled with calculated porosity of each lamination to generate a porosity-lamination map to reflect the porosity changes among laminations (Fig. 13). Although the porosity does not show

a large change within the same lamination, the fractures often related to local tectonic activities can offset the lamination and lead to porosity variation. The local tectonic movement will stimulate the generation of fractures which can offset the a lamination by micrometers to a meter (at scales larger than meters, the fracture is called a fault). In this Eagle Ford sample, the lamination offset is limited to m-mm scales, and it will not impact porosity measurements at the 2.5 cm-diameter core plug scale, but will affect petrophysical analyses at sample sizes at sub-mm scales (e.g., 100s μ m used for gas physisorption, a common approach to determining pore size distribution). However, other studies (Gillen et al., 2019; Zhang et al., 2019; Xu et al., 2020) reported that some lamination offsets can be at the cm-m scale; this large-scale offset will lead to variable results from two cores which are distanced at meters apart.

5. Conclusions

This study investigates the areal heterogeneity of mineral compositions, pore structure, and organic matter composition on two sub-dm-sized samples from an outcrop of Eagle Ford Shale. Even though it is not visible to the naked eye, the spatial heterogeneity can be observed across the whole sample area with the help of μ -XRF and (U)SAXS. Based on the relationship between compositions and measured porosity from (U)SAXS, the porosity at other non-measured locations can be extrapolated; and the sedimentary-textural maps can be associated with calculated porosity. The capabilities of quickly and non-destructively analyzing dm-scaled samples and providing good resolutions of μ m to cm of those two techniques for areal heterogeneity studies open up a wide range of potential applications to many geological fields such as mineralogy, petrology, sedimentary geology, environmental geology, energy geology, and astrogeology.

Acknowledgment

We thank the financial support from the Nuclear Energy University Program managed by the Office of Nuclear Energy at U.S. Department of Energy (award number DE-NE0008797), the Grants-in-Aid program (John H. and Colleen Silcox Named Grant in 2021) of American Association of Petroleum Geologists, and Japan Atomic Energy Agency. The X-ray scattering data were collected at the X-ray Science Division beamline of 9-ID, a resource of the Advanced Photon Source, a U.S. Department of Energy (DOE) Office of Science User Facility operated for the DOE Office of Science by Argonne National Laboratory under Contract No. DE-AC02-06CH11357. All laboratory-derived data presented in this work will be placed into a repository managed by Mavs Dataverse of the University of Texas at Arlington.

References

- Alnahwi, A., Loucks, R., G., 2018. Mineralogical composition and total organic carbon quantification using x-ray fluorescence data from the Upper Cretaceous Eagle Ford Group in southern Texas. *AAPG Bulletin*, 103, 12, 2891-2907.
- Bai, L., Liu, B., Du, Y., Wang, B., Tian, S., Wang, L., Xue, Z., 2021.

Distribution characteristics and oil mobility thresholds in lacustrine shale reservoir: Insights from N₂ adsorption experiments on samples prior to and following hydrocarbon extraction. *Petroleum Science*, in press, <https://doi.org/10.1016/j.petsci.2021.10.018>.

Barker, R, D., Barker, S, L, L., Wilson, S, A., Srock, E, D., 2020a. Quantitative mineral mapping of drill core surfaces I: A method for μ XRF mineral calculation and mapping of hydrothermally altered, fine-grained sedimentary Rocks from a Carlin-type gold deposit. *Economic Geology*, 116, 4, 803-819.

Barker, R, D., Barker, S, L, L., Cracknell, M, J., Srock, E, D., Holmes, G., 2020b. Quantitative mineral mapping of drill core surfaces I: Long-wave infrared mineral characterization using μ XRF and machine learning. *Economic Geology*, 116, 4, 821-836.

Birdwell, J, E., Draves, C., Kemeny, G., Whaley, S., Wilson, S, A., 2019. Application of multiple hyperspectral imaging tools to the examination of submillimeter variability in geochemical reference materials from major, U.S. shale plays. Processing of AAPG Annual Convention and Exhibition, San Antonio, Texas, May 19-22, Search and Discovery Article #90350.

Borrok, D, M., Yang, W., Wei, M., Mokhtari, M., 2019. Heterogeneity of the mineral and organic content of the Tuscaloosa Marine Shale. *Marine and Petroleum Geology*, 109, 717, 731.

Bourdet, J, F, R., Stalker, L., Hortle, A, L., Ryan, C, R., 2020. Tracking mercury contaminant in the subsurface. Processing of Offshore Technology Conference, Kuala Lumpur, Malaysia, August 17-19. Paper #: OTC-30395-MS.

Breyer, J., Wilty, R, H., Tian, Y., Salman, A., O'Connor, K, W., Kurtoglu, B., Hooper, R. J., Daniels, R, M., Bulter, R, W., Alfred, D., 2015. Limestone frequency and well performance, Eagle Ford Shale (Cretaceous), South Texas, Search and Discovery Article #51091.

Chen, S., Han, Y., Fu, C., Zhang, H., Zhu, Y., Zuo, Z., 2016. Micro and nano-size pores of clay minerals in shale reservoirs: Implication for the accumulation of shale gas. *Sedimentary Geology*, 342, 180-190.

Clouter, A., Brown, D., Hohr, D., Borm, P., Donaldson, K., 2001. Inflammatory effects of respirable quartz collected in workplaces versus standard DQ12 quartz: Particle surface correlates. *Toxicological Sciences*, 63, 90-98.

Curtis, M, E., Cardott, B, J., Sondergeld, C, H., Rai, C, S., 2012. Development of organic porosity in the Woodford Shale with increasing thermal maturity. *International Journal of Coal Geology*, 103, 26-31.

Freboung, G., Ruppel, S, C., Loucks, R, G., Lambert, J., 2016. Depositional controls on sediment body architecture in the Eagle Ford/Boquillas system: Insight from outcrops in west Texas, United States. *AAPG Bulletin*, 100, 4, 657-682.

- Gillen, K., Wood, J. M., Sharp, L., Grimison, T., Guerard, B., 2019. Natural and induced structural fabrics in drill-cores from the Montney Formation, western Canada. Processing of William C. Gussow Geoscience Conference, Banff, Canada, October 15-17.
- Hu, Q.H., Ewing, R.P., Rowe, H.D., 2015. Low nanopore connectivity limits gas production in Barnett Formation. *Journal of Geophysical Research – Solid Earth*, 120, 12, 8073–8087.
- Huang, B., Li, L., Tan, Y., Hu, R., Li., 2020. Investigating the meso-mechanical anisotropy and fracture surface roughness of continental shale. *Journal of Geophysical Research – Solid Earth*, 125, e2019JB017828.
- Ilavsky, J., Jemian, P., 2009. *Irena*, tool suite for modeling and analysis of small-angle scattering. *Journal of Applied Crystallography*, 42, 347-353.
- Ilavsky, J., Zhang, F., Andrews, R. N., Kuzmenko, I., Jemian, P. R., Levine, L. E., Allen, A. J., 2018. Development of combine microstructure and structure characterization facility for in situ and operando studies at the Advanced Photon Source. *Journal of Applied Crystallography*, 51, 867-882.
- İnan, S., Badairy, H. A., İnan, T., Zahrani, A. A., 2018. Formation and occurrence of organic matter-hosted porosity in shales. *International Journal of Coal Geology*, 199, 39-51.
- Ko, L. T., Loucks, R. G., Zhang T., Ruppel, S. C., Shao, D., 2016. Pore and pore network evolution of Upper Cretaceous Boquillas (Eagle Ford-equivalent) mudrocks: Results from gold tube pyrolysis experiments. *AAPG Bulletin*, 100, 11, 1693-1722.
- Kuila, U., Prasad, M., 2013. Specific surface area and pore-size distribution in clays and shales. *Geophysical Prospecting*, 61, 341-362.
- Lehrmann, D. J., Yang, W., Sickmann, Z. T., Ferrill, D. A., McGinnis, R. N., Morris, A. P., Smart, K. J., Gulliver, K. D. H., 2019. Controls on sedimentation and cyclicity of the Boquillas and equivalent Eagle Ford formation from detailed outcrop studies of western and central Texas, U.S.A. *Journal of Sedimentary Research*, 89, 629-653.
- Loucks, R. G., Reed, R. M., Ruppel, S. C., Hammes, U., 2012. Spectrum of pore types and networks in mudrocks and a descriptive classification for matrix-related mudrock pores. *AAPG Bulletin*, 96, 6, 1071-1098.
- Ma, L., Dowey, P. J., Rutter, E., Taylor, K. G., Lee, P. D., 2019. A novel upscaling procedure for characterizing heterogeneous shale

- porosity from nanometer to millimetre-scale in 3D. *Energy*, 181, 1285-1297.
- Michot, L. J., Villieras, F., 2006. Surface area and porosity. *Developments in Clay Science*, 1, 965-978.
- Mighani, S., Bernabe, Y., Boulenouar, A., Mok, U., Evans, B., 2019. Creep deformation in Vaca Muerta Shale from nanoindentation to triaxial experiments. *Journal of Geophysical Research – Solid Earth*, 124, 7842-7868.
- Montes-Hernandez, G., Fernandez-Martinez, A., Charlet, L., Tisserand, D., Renard, F., 2008. Textural properties of synthetic nanocalcite produced by hydrothermal carbonation of calcium hydroxide. *Journal of Crystal Growth*, 310, 2946-2953.
- Nikonow, W., Rammlmair, D., 2016. Risk and benefit of diffraction in energy dispersive X-ray fluorescence mapping. *Spectrochimica Acta Part B*, 125, 120-126.
- O'Brien, N. R., 1996. Shale lamination and sedimentary processes. *Geological Society, Special Publications*, 116, 1, 23-36.
- Peng, S., Xiao, X., 2017. Investigation of multiphase fluid imbibition in shale through synchrotron-based dynamic micro-CT imaging. *Journal of Geophysical Research – Solid Earth*, 122, 4475-4491.
- Pommer, M., Milliken, K., 2015. Pore type and pore size distribution across thermal maturity, Eagle Ford Formation, Southern Texas. *AAPG Bulletin*, 99, 9, 1713-1744.
- Reed, R. M., Sivil, J. E., Sun, X., Ruppel, S. C., 2019. Heterogeneity of microscale lithology and pore systems in an Upper Cretaceous Eagle Ford Group circular core, South Texas, U.S.A. *GCAGS Journal*, 8, 22-34.
- Ross, D. J. K., Bustin, R. M., 2008. Characterizing the shale gas resource potential of Devonian-Mississippian strata in the Western Canada sedimentary basin: Application of an integrated formation evaluation. *AAPG Bulletin*, 92, 1, 87-125.
- Shu, Y., Lu, Y., Hu, Q., Wang, C., Wang, Q., 2019. Geochemical, petrographic and reservoir characteristics of the transgressive systems tract of lower Silurian black shale in Jiaoshiha area, southwest China. *Marine and Petroleum Geology*, 129, 105014.
- Tribouvillard, N., Hatem, E., Averbuch, O., Barbecot, F., Bout-Roumazielles, V., Trentesaus, A., 2015. Iron availability as a dominant control on the primary composition and diagenetic overprint of organic-matter-rich rocks. *Chemical Geology*, 401, 67-82.
- U.S. Energy Information Administration, 2022. Drilling productivity report. Department of Energy, Washington, D.C., Accessible at

<https://www.eia.gov/petroleum/drilling/>

Wang, Q., Hu, Q., Larsen, C., Zhao, C., Sun, M., Zhang, Y., Zhang, T., 2021a. Microfracture-pore structure characterization and water-rock interaction in three lithofacies of the lower Eagle Ford Formation. *Engineering Geology*, 292, 106276.

Wang, Q., Hu, Q., Ning, X., Ilavsky, J., Kuzmenko, I., Tom, T., 2021b. Spatial heterogeneity analyses of pore structure and mineral composition of Barnett Shale using X-ray scattering techniques. *Marine and Petroleum Geology*, 134, 105354.

Wang, Y., Liu, L., Hu, Q., Hao, L., Wang, X., Sheng, Y., 2020. Nanoscale pore network evolution of Xiamaling Marine Shale during organic matter maturation by hydrous pyrolysis. *Energy & Fuels*, 34, 1548-1563.

Wu, S., Yang, Z., Zhai, X., Cui, J., Bai, L., Pan, S., Cui, J., 2019. An experimental study of organic matter, minerals and porosity evolution in shales within high-temperature and high-pressure constraints. *Marine and Petroleum Geology*, 102, 377-390.

Xu, S., Gou, Q., Hao, F., Zhang, B., Shu, Z., Zhang, Y., 2020. Multiscale faults and fractures characterization and their effects on shale gas accumulation in the Jiaoshiba area, Sichuan Basin, China. *Journal of Petroleum Science and Engineering*, 189, 107026.

Yang, S., Horsfield, B., 2020. Critical review of the uncertainty of T_{max} in revealing the thermal maturity of organic matter in sedimentary rocks. *International Journal of Coal Geology*, 225, 103500.

Yang, R., He, S., Yi, J., Hu, Q., 2016. Nano-scale pore structure and fractal dimension of organic-rich Wufeng-Longmaxi shale from Jiaoshiba area, Sichuan Basin: Investigations using FE-SEM, gas adsorption and helium pycnometry. *Marine and Petroleum Geology*, 70, 27-45.

Yawar, Z., Schieber, J., 2017. On the origin of silt laminae in laminated shales. *Sedimentary Geology*, 360, 22-34.

Zhang, J., Zeng, Y., Slatt, R., 2019. XRF (X-ray fluorescence) applied to characterization of unconventional Woodford Shale (Devonian, U.S.A.) lateral well heterogeneity. *Fuel*, 254, 115565.

Zhang, W., Yang, W., Xie, L., 2017. Controls on organic matter accumulation in the Triassic Chang 7 lacustrine shale of the Ordos Basin, central China. *International Journal of Coal Geology*, 183, 38-51.

Zhang, X., Shi, W., Hu, Q., Zhai, G., Wang, R., Xu, X., Xu, Z., Meng, F., Liu, Y., 2019. Pressure-dependent fracture permeability of marine shales in the Northeast Yunnan area, Southern China. *International Journal of Coal Geology*, 214, 103237.

Table 1 Results of mineral composition (XRD), TOC (LECO), and pyrolysis (HAWK) for the Eagle Ford Shale samples.

Sample ID	Mineral composition (wt.%)	TOC (wt.%)	Pyrolysis			
	Quartz	Calcite	Pyrite	Clays		S ₁ (mg HC/g)
Powder sample	7.3	91.2	0.8	0.7	N/A	
C3	6.2	93.8		nd	1.4	0.1
C10	6.1	93.9		nd	1.5	0.2
C16	5.2	94.8		nd	1.3	0.3
C21	6.9	91.6	1.6	nd	1.5	0.2
C34	10.8	85.6	3.7	nd	2.2	0.2
C37	11.7	87.0	1.3	nd	2.2	0.2
R15	14.2	84.7	1.1	nd	2.6	0.2
R22	6.3	93.7		nd	1.4	0.2
R24	13.8	84.0	2.3	nd	1.7	0.2
R26	7.6	92.4		nd	1.6	0.2
R28	11.1	88.9		nd	1.9	0.2
R30	15.1	82.7	2.2	nd	2.9	0.3

nd: not detected.

Table 2 Porosity, pore size distribution, surface area and surface area distribution data for six subsample locations in the C and R samples from (U)SAXS analyses.

Sample ID	Position ID	Porosity (%)	Pore size distribution (%)	Surface area (m ² /g)	Surface area distribution (%)
			1-10 nm	10-50 nm	50-100 nm
Circular (C)	3A	1.52	0.37	14.00	6.52
	10B	1.30	0.59	14.36	7.93
	16A	1.08	0.67	17.38	7.37
	21B	1.33	0.52	14.46	7.34
	34A	2.00	0.67	14.75	7.65
	37A	2.43	0.55	8.53	7.22
Rectangular (R)	15A	2.19	0.60	11.52	6.63
	22A	1.22	0.81	14.96	7.59
	24C	1.94	0.65	13.85	7.47
	26A	1.74	0.88	16.10	7.39
	28A	1.73	0.76	16.00	7.24
	30A	2.50	0.76	13.93	7.16

Figure 1. Workflow of sample preparation (A) and experiments at different sampling locations (yellow dots: X-ray scattering; a blue rectangle: thin-section petrographic microscopy; orange squares: XRD, SEM, TOC and pyrolysis) for

Circular (Fig. 1B) and Rectangular (Fig. 1C) samples.

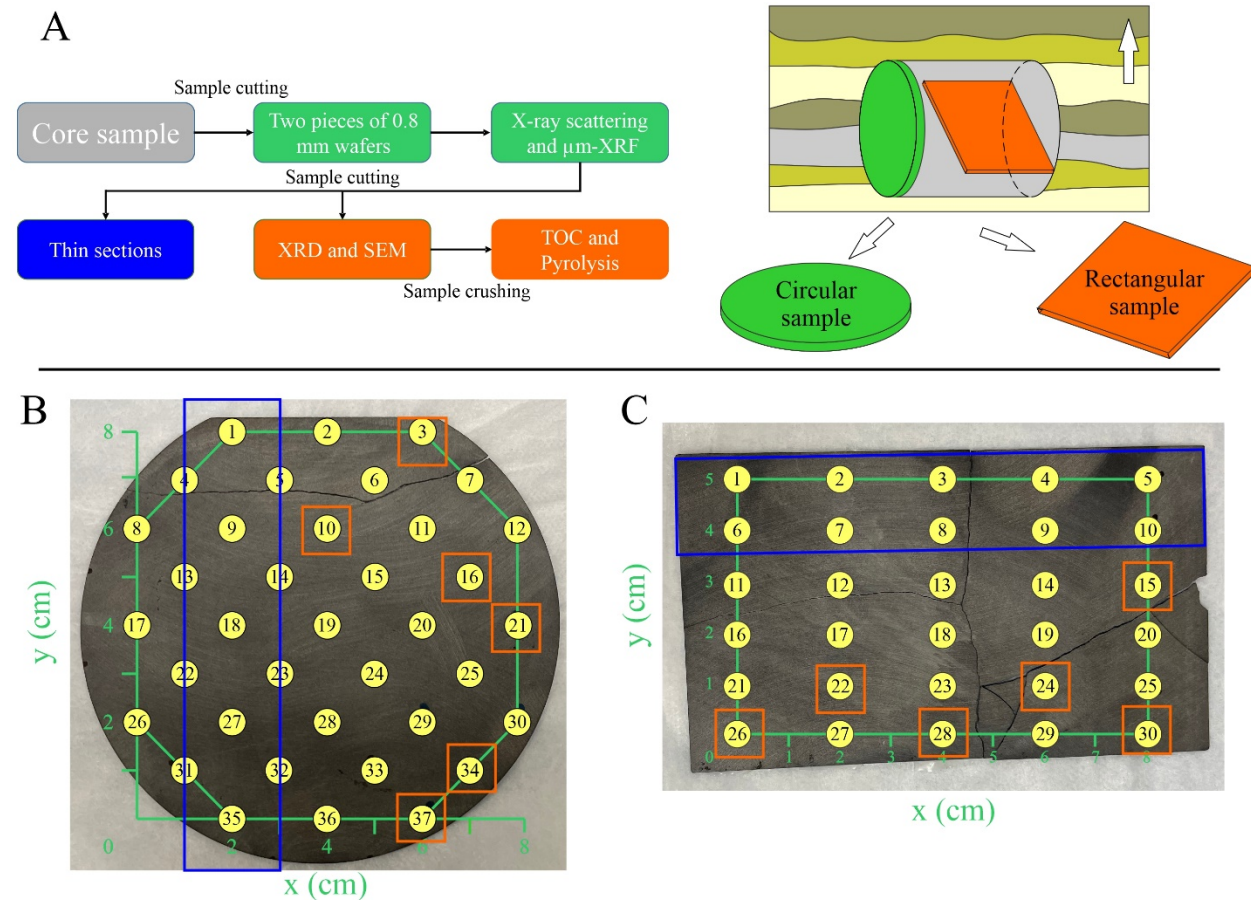


Figure 2. (A) Sample photo and (B-I) elemental distribution of Ca, Si, Mg, Mn, Fe, Al, Na, and K from μ -XRF for the circular-shaped wafer sample (Fig. 1B).

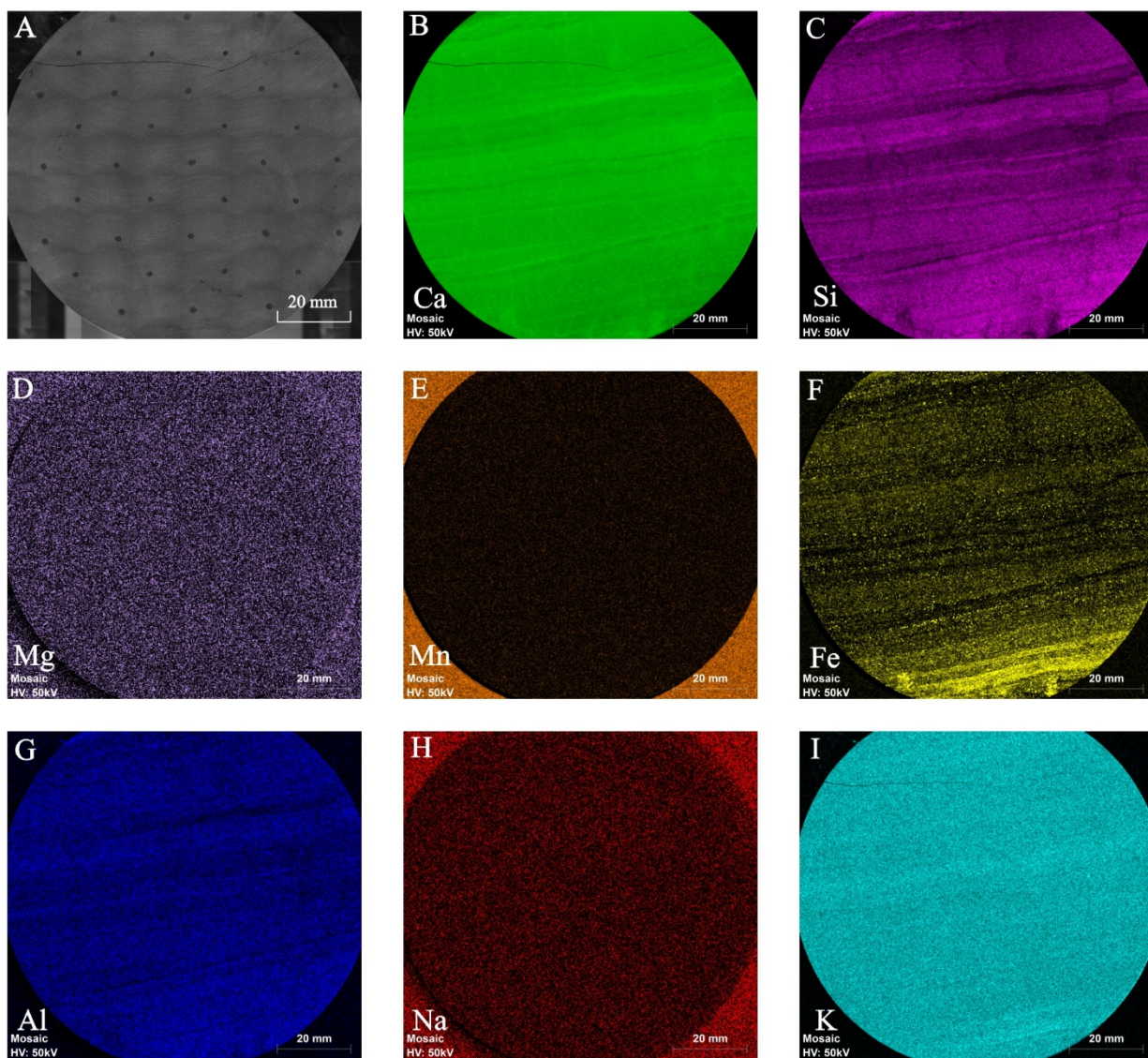


Figure 3. (A) Sample photo and (B-I) elemental distribution of Ca, Si, Mg, Mn, Fe, Al, Na, and K from μ -XRF for the rectangular-shaped wafer sample (Fig. 1C).

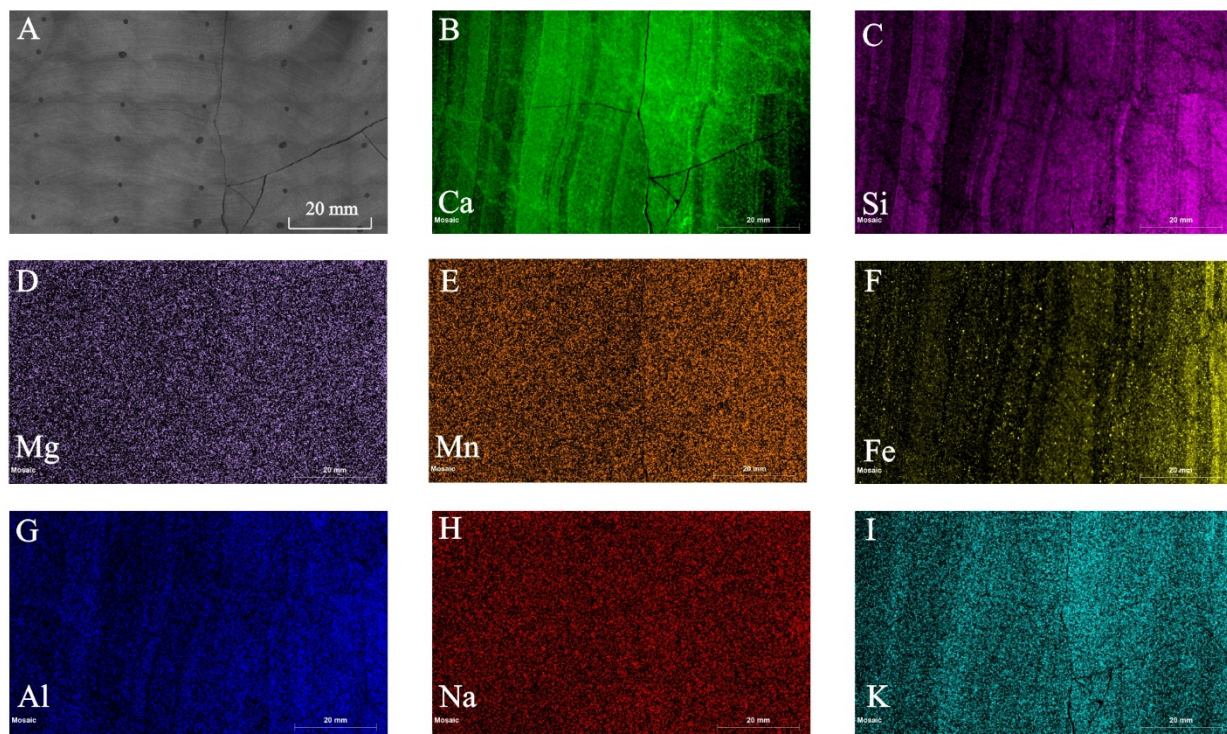


Figure 4. Elemental intensities of Ca, Si, and Fe for (A-C) Circular and (D-F) Rectangular samples as well as the interpretation of sedimentary features (G-H).

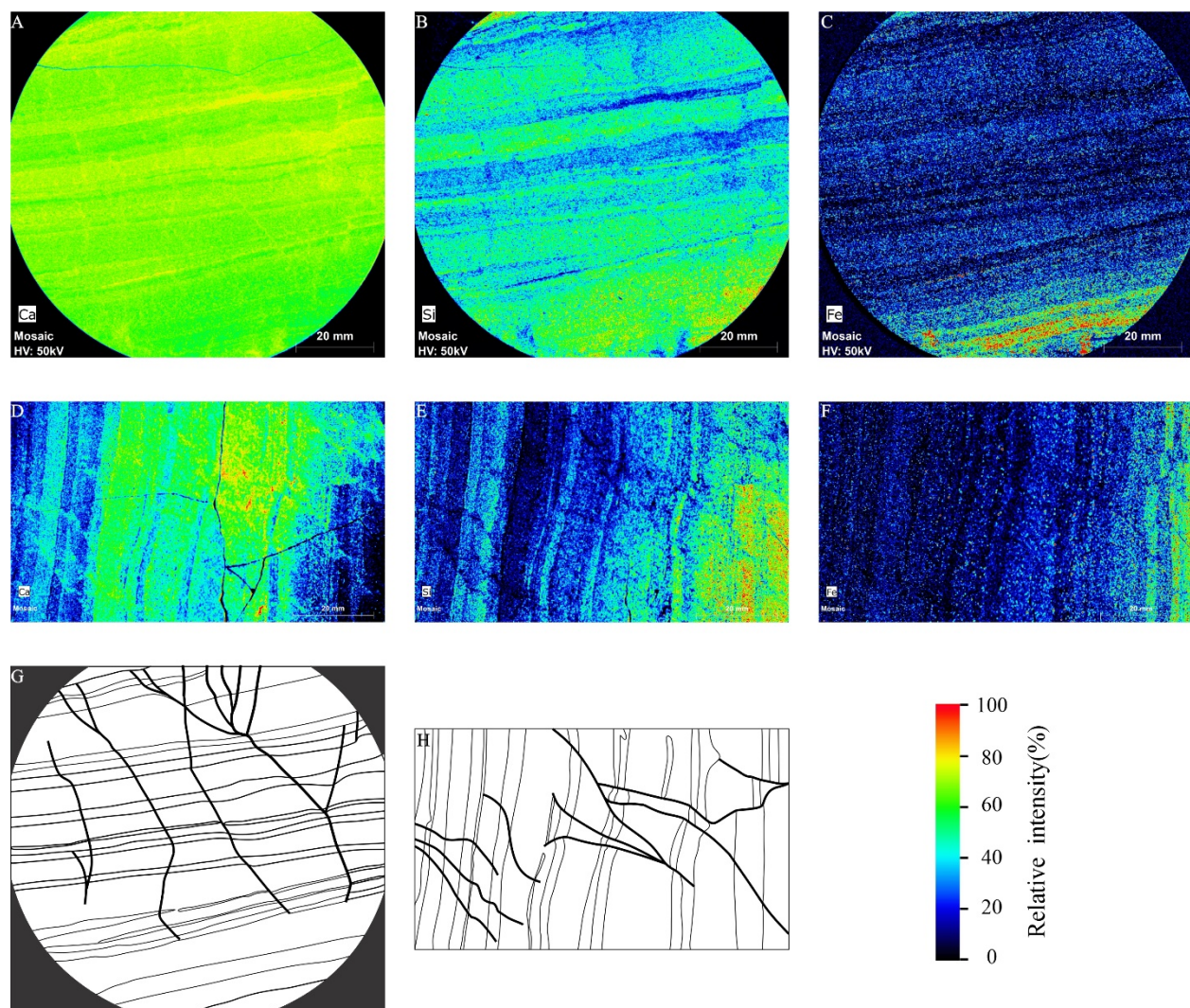


Figure 5. Sampling positions for thin-section petrography (A-H) and analyses of SEM, XRD, TOC, and pyrolysis (Fig. 1B-C).

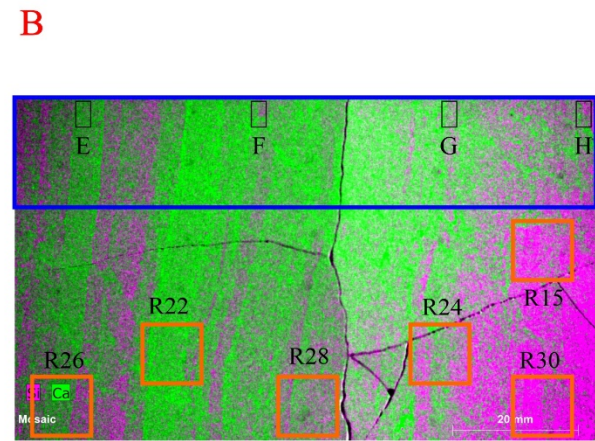
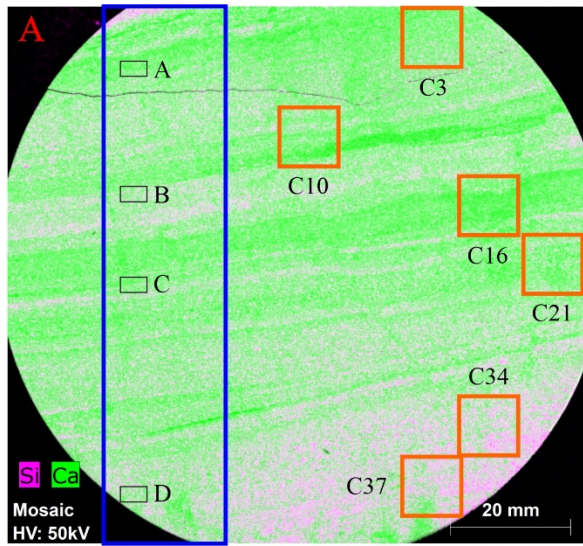
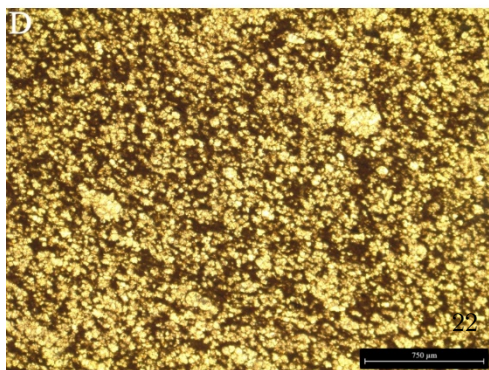
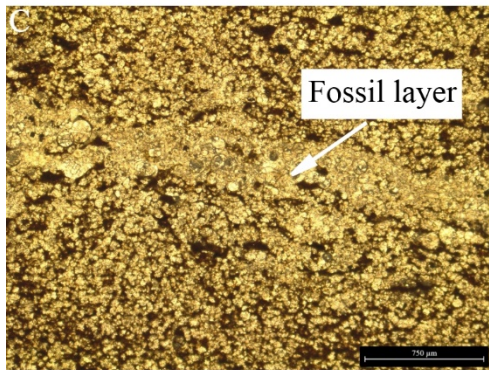
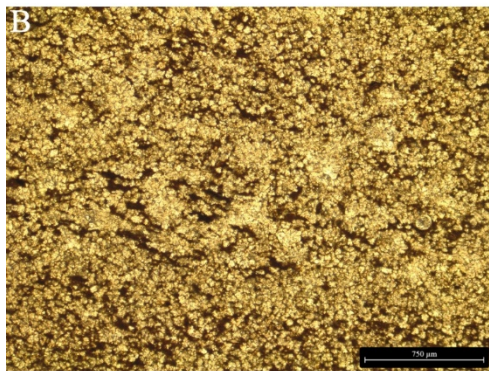
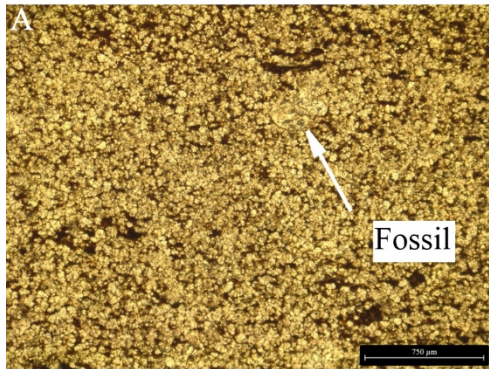


Figure 6. Thin-section petrographic photos of selected positions marked in Figure 5.

Circular sample



Rectangular sample

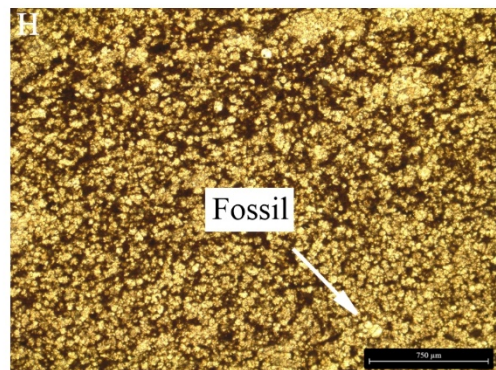
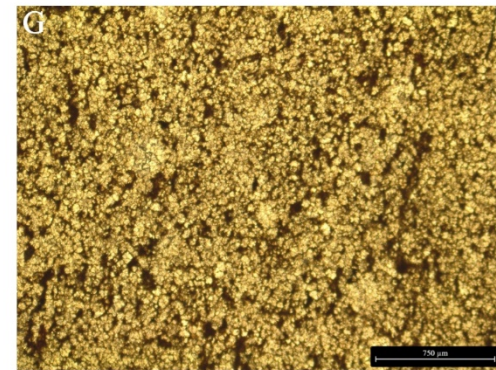
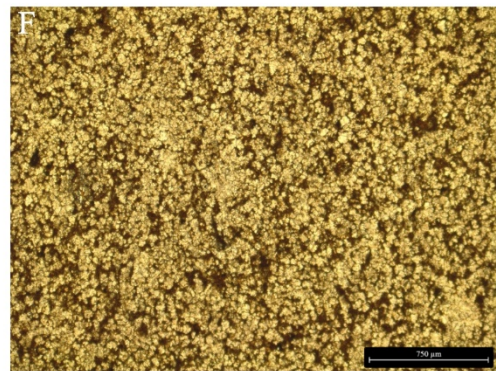
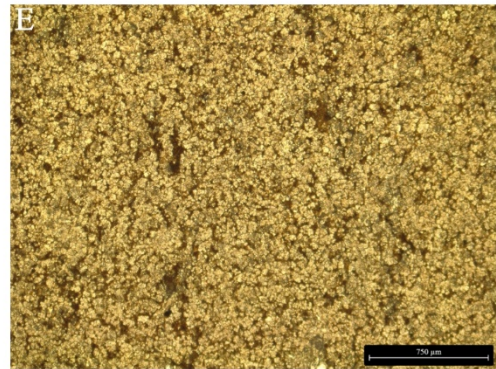


Figure 7. (U)SAXS mapping results of porosity (A-B) and surface area (C-D) distribution for Circular and Rectangular samples of Eagle Ford Shale.

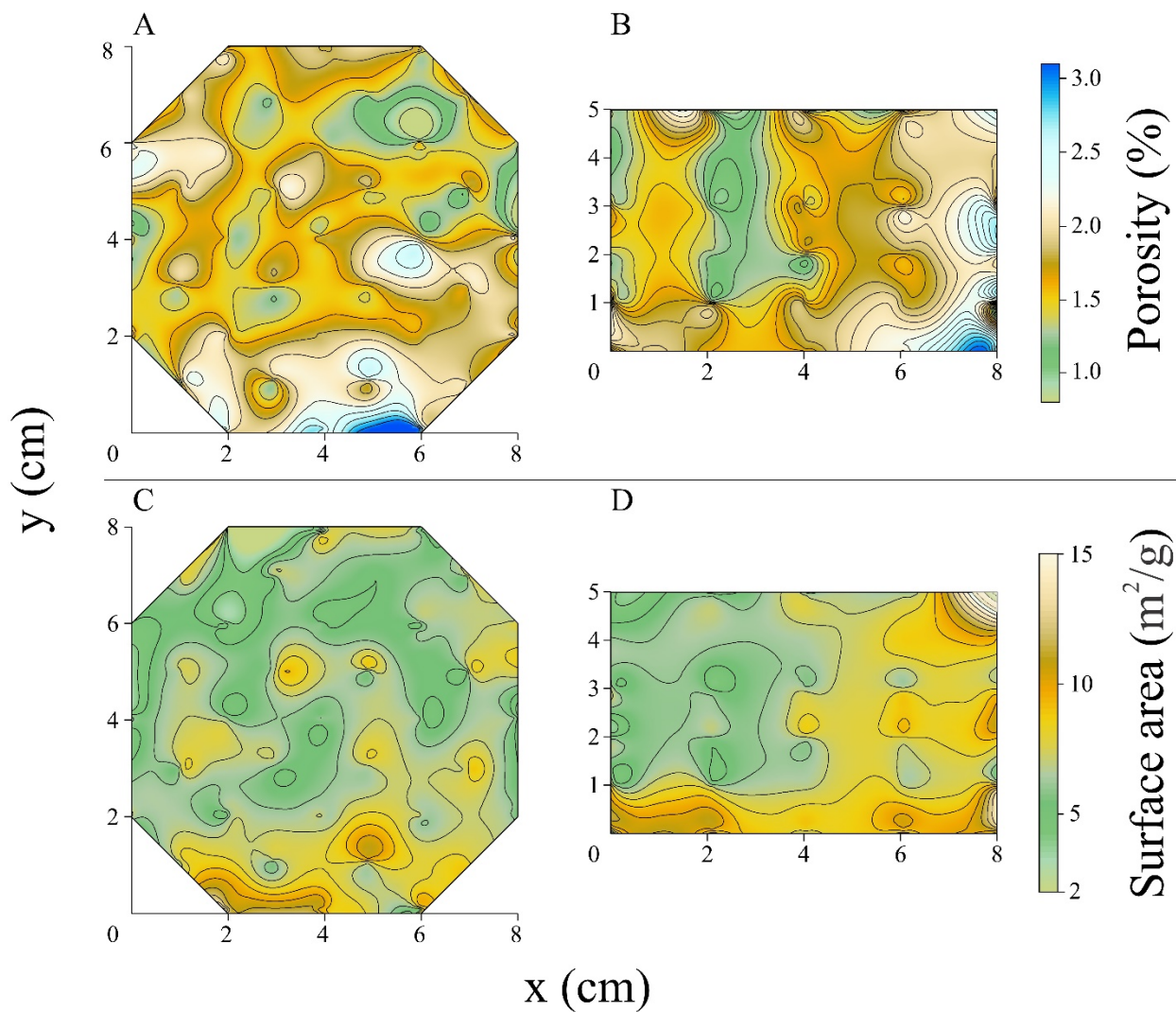


Figure 8. WAXS results for sampling positions of high calcite (A and C) and high siliceous minerals (B and D) in Circular and Rectangular samples.

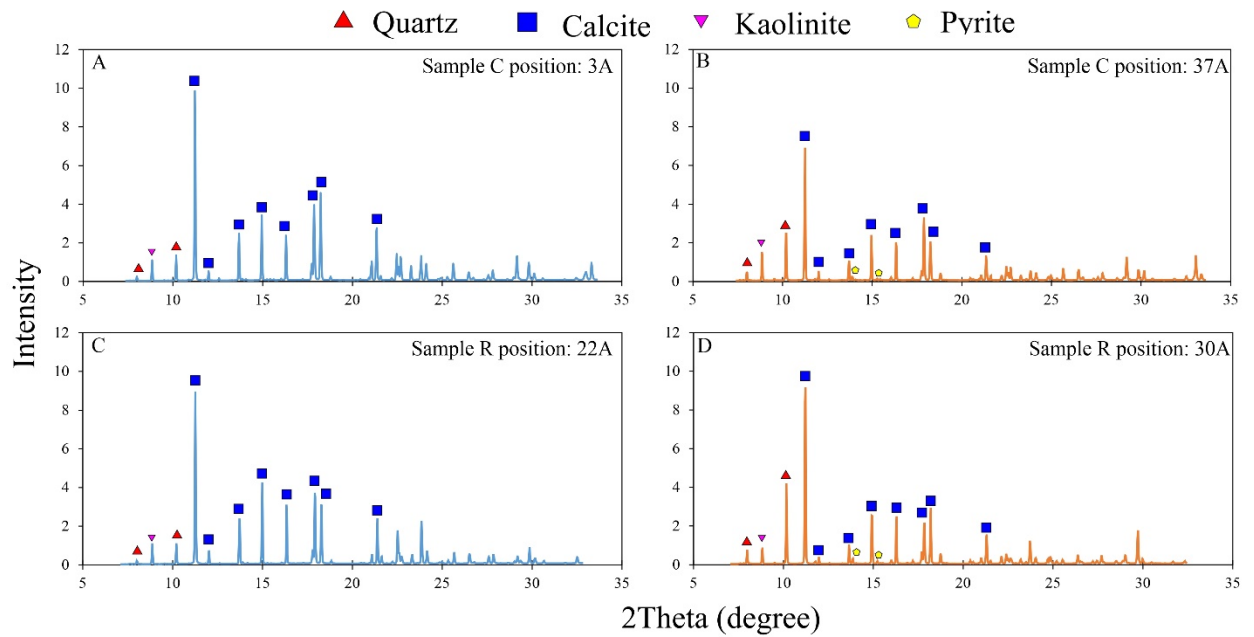


Figure 9. SEM images of the Circular sample: (A) C3, interparticle pores between minerals; (B) C10, interparticle pores and calcite matrix; (C) C16, calcite matrix; (D) C21, interparticle pores between minerals; (E) C34, pyrite; (F) C34, clay minerals and intraparticle pores; (G) C37; organic matter; (H) C37; clay minerals and intraparticle pores; and (I) C37; interparticle pores between minerals.

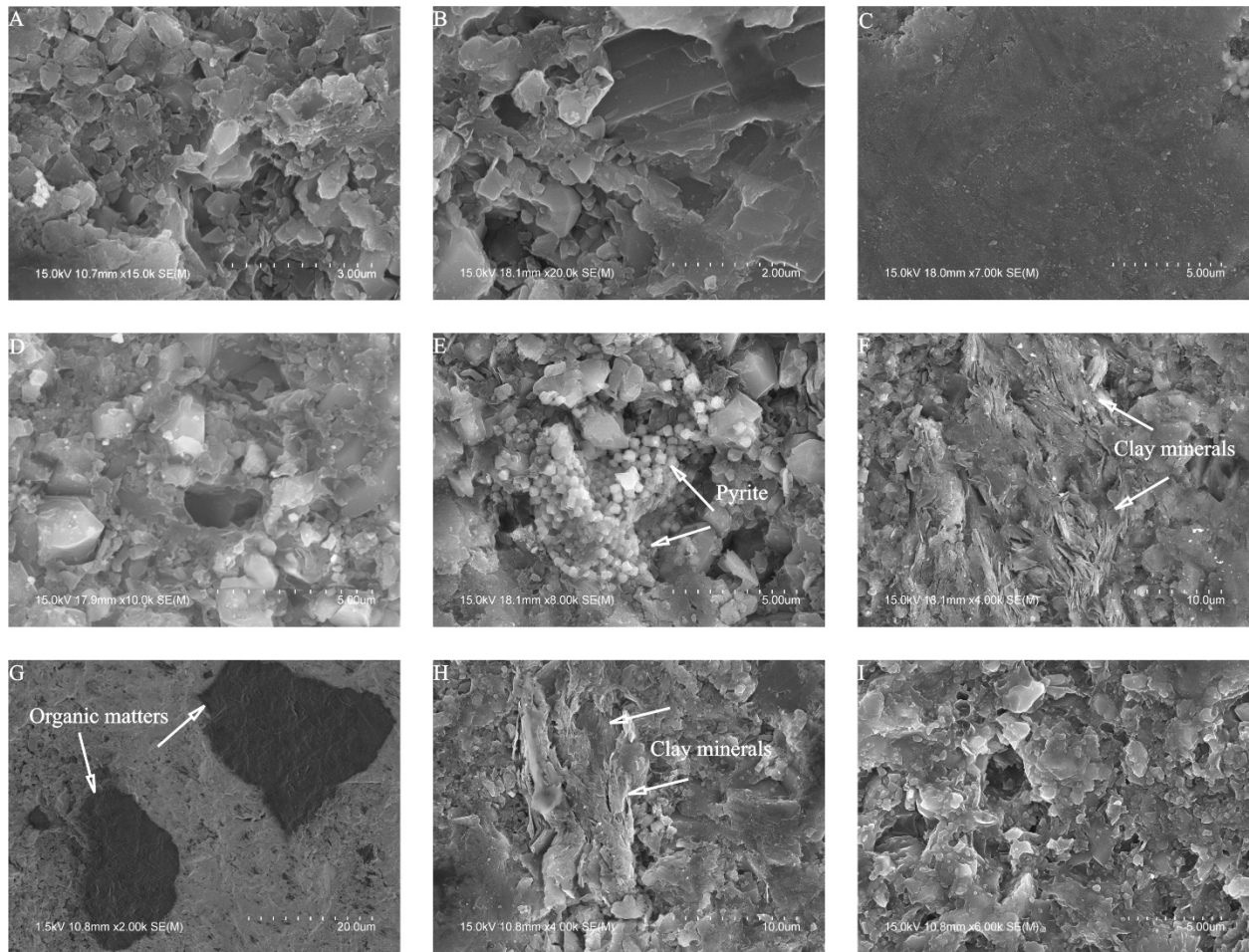


Figure 10. SEM images of the Rectangular sample: (A) R15, pyrite and clay minerals; (B) R22, pores in calcite matrix; (C) R24, interparticle pores and calcite matrix; (D) R26, interparticle pores and calcite matrix; (E) R28, pyrite; (F) R28, organic matter; (G) R28, interparticle pores; (H) R30; pyrites; and (I) R30; clay minerals.

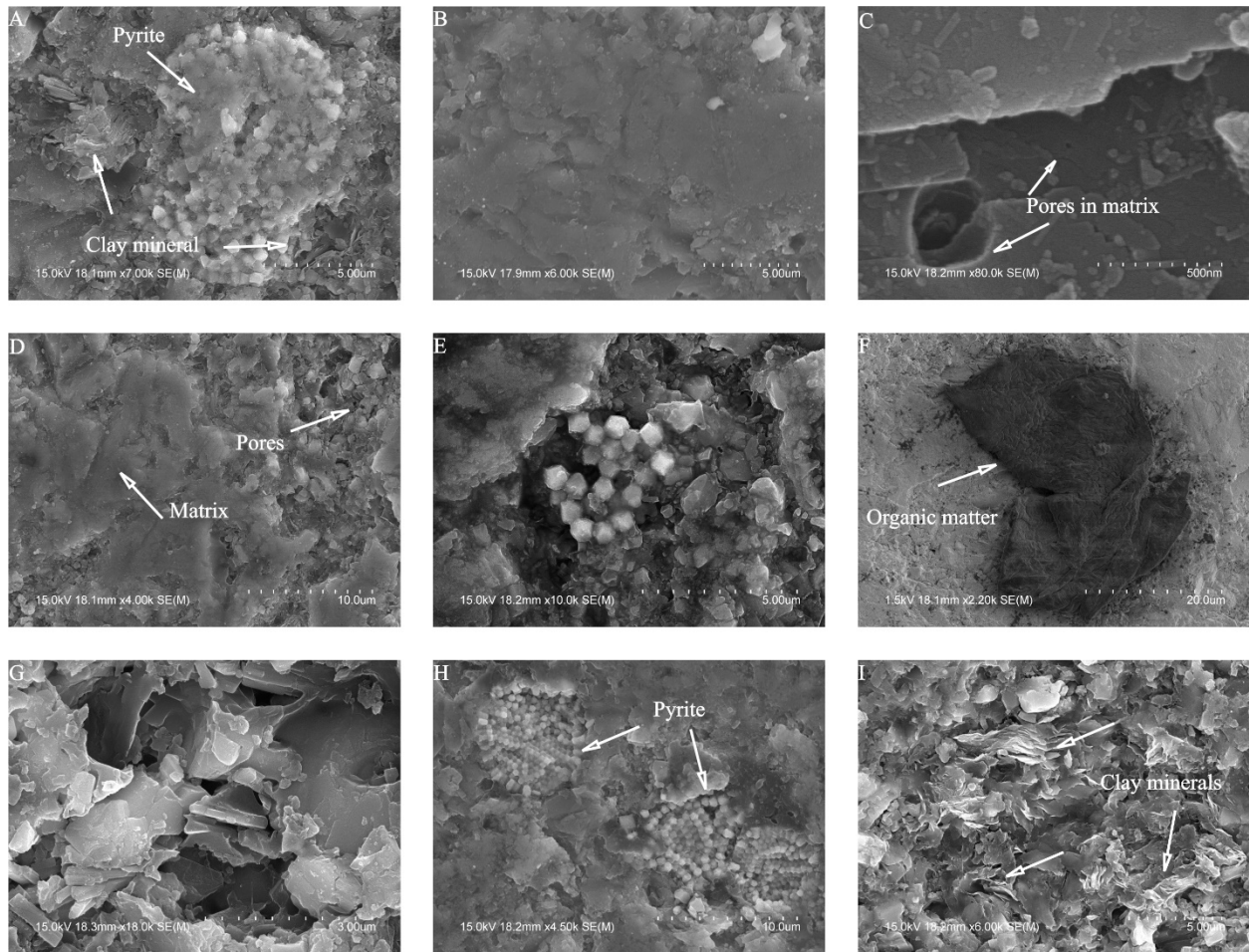


Figure 11. Comparison of porosity (A-B) and surface area (C-D) with pore diameter for six subsample locations on the Circular and Rectangular samples.

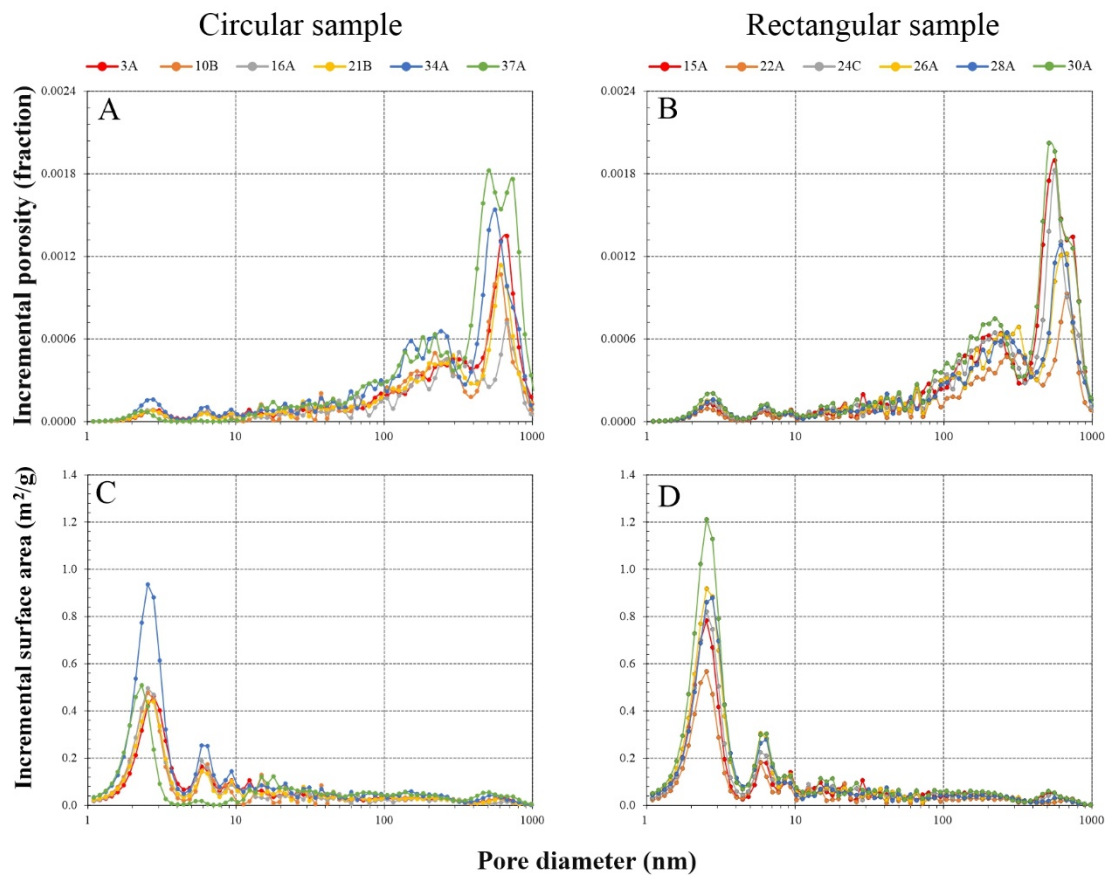


Figure 12. Relationships between calcite content (from XRD) with A: porosity [from (U)SAXS]; B: surface area [from (U)SAXS]; C: TOC (from LECO); and D: S2 (from pyrolysis).

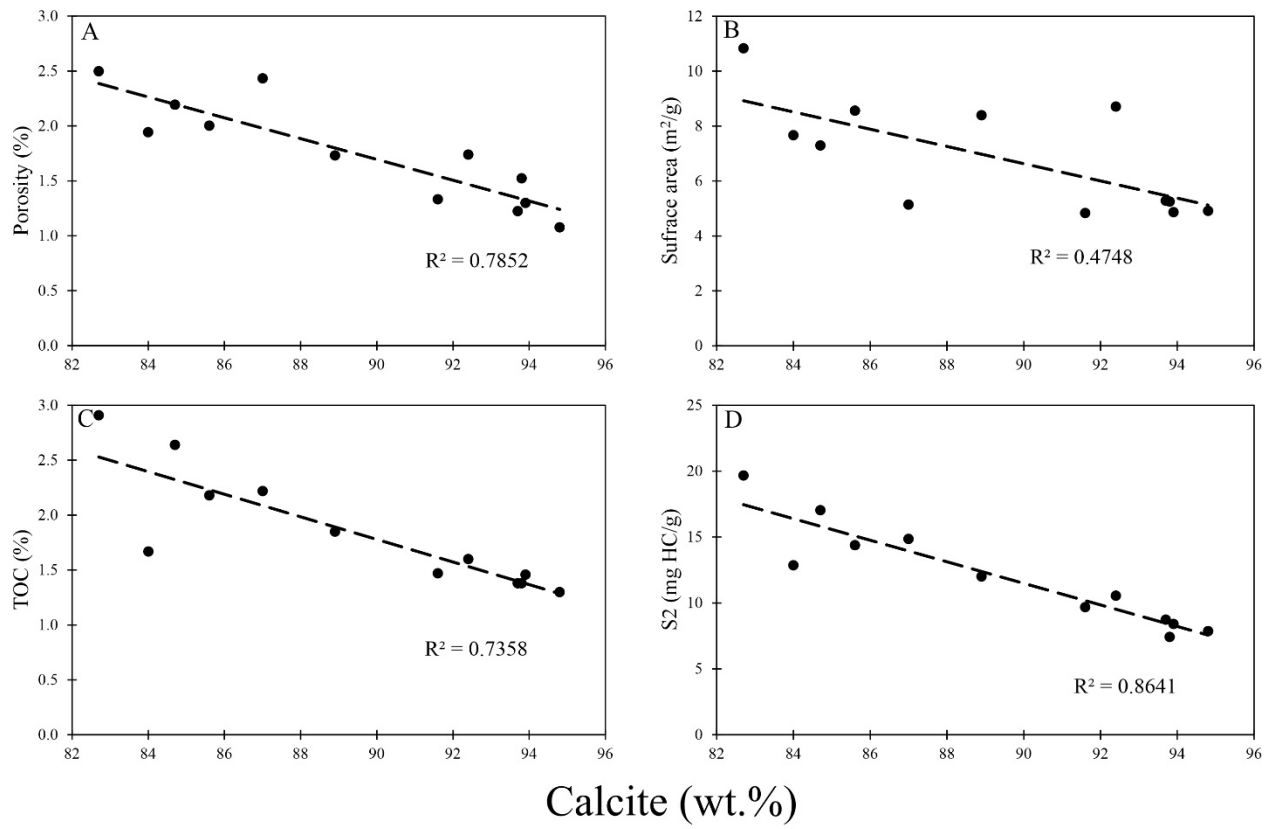


Figure 13. Sub-decimeter-scale areal heterogeneity of porosity distribution and sedimentary features for (A) Circular and (B) Rectangular samples.

